Performance of the RADPHI detector and trigger in a high rate tagged photon beam

R.T. Jones[a,1], T. Bogue[a,2], B.E. Evans[a], M. Kornicer[a], A.R. Dzierba[b], R. Gardner[b,3],
J.L. Gunter[b,4], D. Krop[b], R. Lindenbusch[b], D.R. Rust[b], E. Scott[b], P. Smith[b], C. Steffen[b,5],
S. Teige[b,*], D.S. Armstrong[c], J.H.D. Clark[c,6], L.J. Kaufman[c,7], D.J. Steiner[c], E. Frlez[d],
D. Pocanic[d], J.J. Kolata[e], L.O. Lamm[e], G. Rogachev[e], C. Campbell[f], E. Collins[f],
L. McGlinchey[f], P. Rubin[f,8,9], E. Walker[f], G.S. Adams[g], J. Napolitano[g], H. Crannell[h],
D.I. Sober[h], R.R. Mammei[i,10], E.S. Smith[i]

[a]Department of Physics, University of Connecticut, Storrs, CT 06268, USA
[b]Department of Physics, Indiana University, Bloomington, IN 47405, USA
[c]Department of Physics, College of William and Mary, Williamsburg, VA 23187, USA
[d]Department of Physics, University of Virginia, Charlottesville, VA 22903, USA
[e]Department of Physics, University of Notre Dame, Notre Dame, IN 46556, USA
[f]Department of Physics, University of Richmond, Richmond, VA 23173, USA
[g]Department of Physics, Rensselaer Polytechnic Institute, Troy, NY 12180-3590, USA
[h]Department of Physics, Catholic University, Washington D.C. 20064, USA
[i]Thomas Jefferson National Accelerator Facility, Newport News, VA 23606, USA

Abstract

We describe the design and operation of a detector system for measuring all-photon decays of mesons photoproduced in a tagged photon beam with energies between 4.3 and 5.4 GeV and a flux of 5×10^7 tagged photons per second. Photons from meson decays were detected with a lead-glass calorimeter with an energy resolution of 11% at 1 GeV. Various veto and trigger components were also present. Final states with as many as six photons were successfully detected and reconstructed.
© 2006 Elsevier B.V. All rights reserved.

*Corresponding author. Tel.: +1 812 855 4623.
  E-mail address: steige@indiana.edu (S. Teige).

[1]RADPHI Spokesman, 2001-present.
[2]Present address: Department of Physics, New Mexico State University, Las Cruces, NM 88003, USA.
[3]Present address: Department of Physics, University of Chicago, Chicago, IL 60637, USA.
[4]Present address: Departments of Diagnostic Radiology and MR Research Laboratory, Mayo Clinic, Rochester, MN 55905, USA.
[5]Present address: National Center for Supercomputing Applications, Urbana, IL 61801, USA.
[6]Present address: American Physical Society, One Physics Ellipse, College Park, MD 20740, USA.
[7]Present address: U. Massachusetts Amherst, Amherst, MA 01003, USA.
[8]Present address: Department of Physics and Astronomy, George Mason University, Fairfax, VA 22030, USA.
[9]RADPHI Spokesman, 1998–2001.
[10]Present address: Department of Physics, Virginia Polytechnic Institute and State University, Blacksburg, VA 24061, USA.

1. Introduction

The all-neutral detector built for the RADPHI experiment [1] at the U.S. Department of Energy's Thomas Jefferson National Accelerator Facility (Jefferson Lab) was designed to detect and measure all-photon decays of ϕ mesons photoproduced in a 50 MHz tagged bremsstrahlung photon beam. The major component of this detector was a 620-element lead-glass electromagnetic calorimeter. This paper describes the design and operation of the detector. The performance of a detector with the capability of reconstructing all-neutral decays in a high rate bremsstrahlung photon beam environment is of particular interest to future experiments with photon beams.

The Continuous Electron Beam Accelerator Facility (CEBAF) at Jefferson Lab is able to produce high quality photon beams via incoherent or coherent bremsstrahlung [2]. These photon beams are characterized by high fluxes, high duty factor and superior emittance and make possible, for the first time, high statistics studies of peripherally produced mesons. Indeed, a significant component of the planned physics program at an energy-upgraded CEBAF [3] involves the photoproduction of exotic hybrid mesons.

Incident photons are expected to be particularly effective in producing these states. In addition, the relatively large cross-section for diffractive photoproduction of vector mesons, such as the ϕ meson, creates the opportunity to study their rare radiative decays.

The primary goal of the RADPHI experiment was to measure radiative decays of the ϕ meson, $\phi \to M\gamma$, where M is a pseudoscalar meson such as the π^0 or η, or a scalar meson such as the $f_0(980)$ or $a_0(980)$. The decays involving the scalars are rare with branching ratios of order 10^{-4} [4]. The cross-section for ϕ photoproduction ($\approx 0.5\,\mu b$) combined with these small branching ratios requires an experiment that can operate with photon beam intensities as high as possible. A list of all-neutral meson decays that are accessible to the RADPHI experiment is given in Table 1.

It is seen that all of the decays in Table 1 lead to a final state consisting solely of photons. At photon beam energies above $\approx 3\,\text{GeV}$ where t-channel reactions are dominant, most of the final-state photons are produced at forward angles in the laboratory frame. Thus a detector for these decays must have sufficient spatial resolution to distinguish several closely spaced electromagnetic showers in the region close to the forward direction. In the RADPHI experiment, this was accomplished using the Lead-Glass Detector (LGD). In most cases, the photoproduction of a vector meson from a proton target occurs at very forward angles, with a low-energy (typically less than 0.5 GeV kinetic energy) recoil proton emerging at a large angle (typically 40–60°) to the beam direction. Reactions in which the recoil proton is the only charged particle in the final state comprise less than 10% of the total photoproduction cross-section at these energies. The RADPHI experiment used scintillation counters surrounding the target to detect these recoil protons and insure that no

Table 1
Primary meson decays to all-neutral final states

Decay	Photon multiplicity
$\pi^0 \to 2\gamma$	2γ
$\eta \to 2\gamma$	2γ
$\eta \to 3\pi^0$	6γ
$\rho \to \pi^0\gamma$	3γ
$\rho \to \eta\gamma$	3γ
$\omega \to \pi^0\gamma$	3γ
$\omega \to \eta\gamma$	3γ
$\eta' \to 2\gamma$	2γ
$\eta' \to 2\pi^0\eta$	6γ
$\sigma/f_0(980) \to 2\pi^0$	4γ
$a_0(980) \to \eta\pi^0$	4γ
$\phi \to \eta\gamma$	3γ
$\phi \to a_0(980)\gamma \to \eta\pi^0\gamma$	5γ
$\phi \to f_0(980)\gamma \to 2\pi^0\gamma$	5γ
$b_1(1235) \to \omega\pi^0$	5γ
$a_1(1260) \to 3\pi^0$	6γ
$f_2(1270) \to 2\pi^0$	4γ
$f_1(1285) \to \eta 2\pi^0$	6γ
$a_2(1320) \to \eta\pi^0$	4γ

other charged particles were present in the event. A gamma veto counter covered the region at laboratory angles beyond the coverage of the LGD to reject events with extra photons at large angles.

2. Accelerator and photon beam line

The CEBAF accelerator at Jefferson Lab is a five-pass recirculating linear accelerator, with superconducting radio-frequency cavities in its two straight sections. The accelerator delivered an electron beam of energy 5.65 GeV to experimental Hall B for this experiment.

A photon beam was generated by bremsstrahlung of electrons striking a thin gold foil. In the early portion of the run a foil of thickness 3×10^{-4} radiation lengths was used. Later, due to concerns regarding electron beam dump heating, the thickness was doubled to maintain the same photon flux at a lower electron beam current. The energy of individual photons was measured by energy analysis of the post-bremsstrahlung electrons using the Hall B tagged photon system [2]. For the RADPHI run only the portion of the tagging range between 4.38 and 5.38 GeV (counters 1–19) was used. The electron beam current was selected such that the total photon rate within this tagging range was 5×10^7 per second.

The photon beam remained in vacuum for about 10 m beyond the tagger. It then emerged through a thin window into a 30-m long polyethylene bag filled with helium. The bag terminated a few centimeters upstream of the RADPHI target. Monte Carlo studies and early beam tests indicated that this helium bag was a satisfactory solution to the problem of background generated by the beam passing through air. The distance from the radiator to the target

was 40 m. The photon beam dump was downstream of the RADPHI apparatus.

3. Experiment hardware

3.1. Detector overview

The RADPHI detector is shown schematically in Fig. 1 and its major components are listed in Table 2.

The beam was incident on a 2.87-cm diameter, 2.53-cm long cylindrical beryllium target. These dimensions were
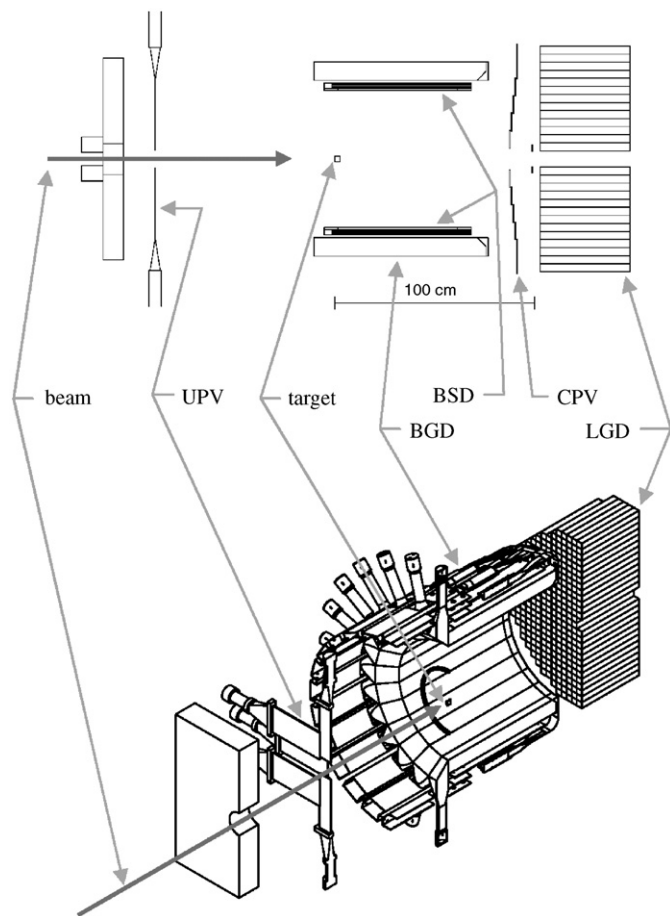

Fig. 1. Cut-away views of the RADPHI detector. In the 3D (lower) view the CPV detector has been omitted to reveal the lead-glass array and the BSD has been omitted to reveal the BGD. All detector subsystems are shown in the 2D (upper) view.

chosen on the basis of GEANT Monte Carlo studies which took into consideration beam size, recoil energy loss, and detector rates. The target was suspended, centered on the beam axis, with three 28 AWG steel wires from a 50 cm diameter Plexiglas ring. A computer-controlled stepper motor could rotate the ring about an axis on its circumference allowing the target to be moved relative to the fixed beam. This capability allowed beam-target scans to be performed without access to the apparatus.

Surrounding the target and extending forward to $30°$ from the beam axis was a cylindrical barrel scintillator detector (BSD) which provided nearly full angular coverage for recoil protons. Surrounding the BSD was a cylindrical barrel gamma detector (BGD) composed of a lead-scintillating fiber matrix, which was used off-line to reject events with large-angle photons.

The primary detector component was a 620-channel lead-glass wall (LGD) assembled to approximate a circle around the beam line with a $8 \times 8 \, cm^2$ central hole for the passage of the beam. The gain of individual calorimeter cells was monitored by a system based on a pulsed nitrogen laser.

A 30-channel scintillator array (charged particle veto, CPV), used to veto charged particles in the final state, was located upstream of the lead-glass array. The CPV was applied during the off-line analysis because rates in the CPV were too high to permit its inclusion in the on-line trigger.

Upstream of the target and all detectors was a 10-cm thick shield wall made of lead poured into a steel jacket. A hole through the wall permitted the photon beam to pass to the target. Mounted upstream of the wall was the lead and steel collimator shown in the second panel of Fig. 1, with inner diameter 6.5 cm, larger than the beam but smaller than the beam hole through the LGD. A scintillator hodoscope (upstream pair veto, UPV) was placed just downstream of this wall in order to veto beam halo interactions on the inner surface of the collimator. The hodoscope consisted of six horizontal and two vertical paddles, arranged around a square opening the size of the helium bag.

In the following sections each detector element is described in more detail. In these descriptions, a right-handed coordinate system is used with the origin at the center of the upstream face of the target with the z-axis along the beam direction and the y-axis up.

Table 2
Glossary of detector subsystems

Symbol	Full name	Description
LGD	Lead-Glass Detector	A circular array of 620 $4 \times 4 \times 45 \, cm^3$ lead-glass blocks
BSD	Barrel Scintillator Detector	A three-layer cylindrical scintillator array surrounding of the target
BGD	Barrel Gamma Detector	A cylindrical lead-scintillating fiber array surrounding the BSD
CPV	Charged Particle Veto	A plane scintillator hodoscope covering the face of the LGD
UPV	Upstream Pair Veto	A scintillator array surrounding the beamline upstream of the target

3.2. The barrel detectors (BGD and BSD)

Two concentric barrel-shaped detectors surrounded the target, both originally built for the Jetset experiment [5,6]. They detected particles emerging from the target between 30° and 90° from the beam axis. The BSD was a hodoscope made up of three concentric cylinders. The innermost layer, of inner radius 35 cm, consisted of 12 paddles twisted to spiral around the barrel in a clockwise direction (looking downstream). The middle layer, of inner radius 36 cm, consisted of 12 paddles twisted to spiral counterclockwise. The outermost layer, of inner radius 37 cm, was composed of 24 paddles all parallel to the beam axis. The scintillators were 0.5 cm thick. The active area of the BSD extended from $z = -2$ to 68 cm and had full azimuthal coverage. A coincidence between counters in all three layers was used to define a triangular region, called a pixel, which enabled the recoil particle direction to be reconstructed in the off-line analysis. All 48 paddles were instrumented with Thorn-EMI 9954 phototubes.

Surrounding the scintillator array was the lead-scintillating fiber calorimeter. The BGD was installed in RADPHI to detect photons that emerge at large angles beyond the solid angle of the forward calorimeter. The fibers ran parallel to the z-axis and extended from $z = -11$ to 75 cm. The detector was segmented azimuthally into 24 counters, each of which was read out on both ends. Upstream light readout was accomplished with 90°-bend light guides, the light being measured with Philips XP2020 phototubes. Constrained to fit into a small space just upstream of the forward detectors, the downstream light collection system consisted of a pad of Bicron (BCF-92), 1.5-mm square, multi-clad wave-shifting fibers positioned at the end of the scintillating fibers. Light from the wave-shifting fibers was detected by Thorn-EMI 9954 phototubes. The thickness of the BGD was 9.3 cm which amounts to about 5.8 radiation lengths at normal incidence. The inner radius of the counter was 39 cm.

3.3. The charged particle veto

The CPV scintillator hodoscope was installed upstream of the lead-glass wall to tag charged particles. The hodoscope shadowed the upstream face of the lead-glass stack and so provided the capability of vetoing (off-line) events that contained charged particles in the final state. It was made up of 30 horizontal paddles, 15 to the left and 15 to the right of center. The paddles were arranged so that neighbors overlapped both vertically and at the center as shown in Fig. 1 (except, of course, around the beam hole). The CPV scintillators were 0.4 cm thick and were staggered in z around a plane at $z = 90$ cm.

The paddles closest to the beam were narrower to approximately equalize rates in the counters. Rates were high enough to require that zener diode bases be installed on the outer 16 paddles and transistorized bases be installed on the inner 14. To further reduce the rate-

dependence of the gain in these counters, the phototube voltages were set at the low end of the efficiency plateau and signals were amplified by a 5× amplifier before being split and analyzed. The phototubes were Thorn-EMI 9214B's.

3.4. The lead-glass detector

The LGD allowed reconstruction of photon energy and momentum from decays of particles of interest to RADPHI. The techniques used to calibrate this detector and to determine its resolution are described elsewhere [7]. After calibration, the LGD achieved an energy resolution of

$$\frac{\sigma_E}{E} = \frac{7.3\%}{\sqrt{E}} + 3.5\% \tag{1}$$

and a position resolution of

$$\sigma_x = \frac{0.64\,\text{cm}}{\sqrt{E}} \tag{2}$$

with E in GeV.

The active elements of the array were lead-glass bars recycled from the Brook-haven National Lab (BNL) E852 detector [8]. The dimensions of the bars were 4 cm × 4 cm × 45 cm. The long axis was oriented parallel to the beam. The bars were wrapped in 0.0005 in. thick aluminized mylar and stacked in a 28 × 28 matrix with the corners removed so as to approximate a circular configuration (see Fig. 1). The four central blocks were removed to permit the unscattered photon beam to pass to the beam dump. A one-piece support structure held the phototubes in place relative to the lead-glass array, one tube per block, with an air gap for coupling. The entire assembly was enclosed in a light-tight box of Herculite.

The gain of the calorimeter cells was monitored by a monitoring system based on a pulsed nitrogen laser. This laser illuminated a 1 cm³ piece of plastic scintillator. Light from this scintillator was propagated along fibers to the edges of a 1×1 m² sheet of Plexiglas covering the upstream face of the LGD. Most of this light was trapped by total internal reflection but a sufficient amount scattered out of the sheet to provide an illumination of the detector sufficient for monitoring purposes. The illumination was found to be uniform to within a factor of two by measuring the intensity of scattered light with a single phototube scanned over the surface of the sheet.

3.5. Radiation damage

Online monitoring of the LGD during the experiment indicated that the gain in the eight blocks immediately adjacent to the beam hole decreased as the run progressed. This observation was based upon the laser monitor system, the raw pulse-height distributions, and the channel gains which were periodically determined during the run. A similar effect was seen, but to a lesser degree, for the next ring of blocks once removed from the beam hole.

During a pause in the experiment, visual inspection of the blocks indicated that the glass was darkening, a well-known effect of radiation damage on lead glass. Fig. 2 illustrates the gain reduction with beam time (roughly proportional to integrated radiation dose) for a typical block adjacent to the beam hole. It is apparent that the gain change is a gradual, cumulative effect rather than a sudden change which might be characteristic of a beam mis-steering event.

The magnitude of the gain loss (order 40%) was such that it could be compensated by adjustments of the PMT high voltages. This was done periodically during the experiment. The last datum in Fig. 2 shows the result of one adjustment. However, this is only a partial solution, since a radiation damaged block produces fewer photo-electrons in the PMT, resulting in a degraded energy resolution which cannot be compensated by increasing the PMT gain. Thus it was desirable to "heal" the radiation damage as much as possible.

Radiation damage in lead glass is known to be temporary and to largely heal itself on the time scale of a few months. The healing can be accelerated by the use of ultraviolet (UV) light. This approach was adopted for the most affected blocks. During an extended down-time in the run, the PMT and base for selected blocks were removed and a UV light guide attached to a quartz-envelope mercury vapor lamp was inserted. The output of the lamp was $5\,\mathrm{W/cm^2}$ in the range 300–480 nm, with a peak intensity at 365 nm. The affected blocks were each illuminated for periods of 6–8 h. These blocks showed a gain increase of 30% following this treatment, nearly recovering their initial performance.

It should be noted that the change in the response of the blocks due to radiation damage and the gain recovery following UV treatment were even more dramatic in the data from the laser monitoring system (typically a factor of two change). The difference between the shift in the pulser response and that seen in the gain constants from the calibration can be qualitatively understood by noting that the laser illuminated the front of the block and thus probed the transmission of the entire block, while the showers seen in the calibration data created Cherenkov light throughout the volume of the block, and were therefore less sensitive to attenuation effects in the upstream region of the block. The radiation damage is expected to be concentrated within one or two radiation lengths of the front surface of the detector, and this was confirmed by visual inspection, in qualitative agreement with the difference between the laser monitor data and the calibration data.

3.6. Electronics

Photon tagger signals were discriminated with Phillips 715 constant fraction discriminator modules and the digital signals were brought to TDCs at the opposite end of the hall along $57.9 \pm 0.3\,\mathrm{m}$ RG-58 cables. A logical OR of signals from the tagger hodoscope was sent through a 0.84c propagation-speed coaxial cable, type LM-240, via a shorter route to the trigger electronics.

Signals from all RADPHI detectors except the lead-glass array were split by impedance-matching splitters. The signals from the LGD were cabled directly into the ADCs. One set of splitter outputs was sent through RG-174 cable to discriminators. The discriminator for the upstream hodoscope was the LeCroy 3412; for the barrel scintillator array, the LeCroy 3412A; for the barrel lead-scintillating fiber calorimeter, the LeCroy 3420 (constant-fraction); and for the charged-particle hodoscope, the LeCroy 4413. Discriminator outputs went to LeCroy 1877S FASTBUS TDCs operated in common stop mode, Struck 7200 VME scalers, and, in some cases, the trigger logic. The other set of outputs was sent through RG-58 cable to custom made, 12-bit, integrating ADCs developed by Indiana University for E852 [9]. During the first 16 ns of the gate, the ADC sampled the signal baseline. It then integrated the signal relative to this baseline for the remaining ∼100 ns of the gate. The integrated charge was discriminated against two independent thresholds for use in higher level triggers, and digitized with a 12-bit successive approximation digitizer.

Digitization began 750 ns after the end of a gate and took 4 μs.

The two discriminators on each channel were designated as the "high" and "low" discriminators corresponding to their programmed thresholds. The thresholds of all ADC discriminators was set during initialization of a data-taking period. The state of the two discriminators was represented as bits in the data stream written by the data acquisition system and also presented on the auxiliary FASTBUS backplane ∼100 ns after the end of the gate. Both
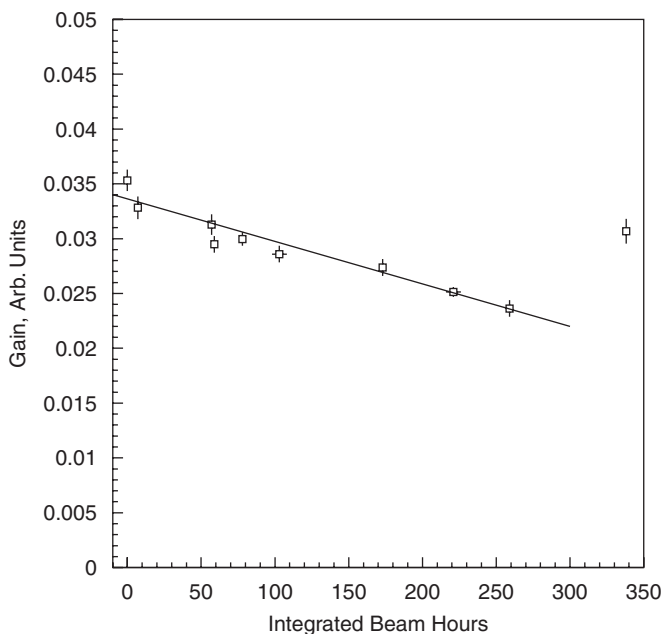

Fig. 2. The effect of radiation damage on the central part of the detector. The last point shows the gain improvement after an adjustment of the phototube high voltage.

sets of discriminators were used in the trigger as described below.

The ADCs were read out in FASTBUS block-transfer mode. To reduce event size, only ADC channels with values at least 5 counts above pedestal were recorded. The typical pedestal r.m.s. width was 0.6 count.

3.7. Trigger

The RADPHI experiment employed a three-level trigger (see Fig. 3), described below. The first level was a logical coincidence of the signals from the barrel scintillator array and photon tagger, in anti-coincidence with the upstream veto array, during the LIVE condition from the hardware trigger supervisor. When the first level trigger condition was satisfied, the electronics generated gates for the ADCs and common-stop signals for the TDCs, initiated the second level trigger processing, and blocked further triggers until additional logic decided to reject or read out the event.

The second level trigger requirement was a logical OR of the levels from the LGD ADC "high" discriminators. This requirement selected events with at least one element of the LGD containing a minimum amount of energy, set to 200 MeV. In the case the level-2 trigger was not satisfied, the ADCs and TDCs were reset, requiring 250 ns before another trigger was allowed. The total incurred dead time for a level-1 trigger that was rejected at level-2 was about 1.2 μs. This reset time was the largest single source of dead time in the experiment.

The third level trigger was a digital sum of the total energy in the lead-glass calorimeter. The sum was computed by a processor module [8,9] designed and built by Indiana University for BNL E852. An 8-bit representation of the energy sum was presented to a LeCroy 2372 memory lookup unit where the value was compared to a threshold value equivalent to roughly 3 GeV.

In the event the level-3 trigger was not satisfied, a clear was sent to the TDCs. The ADCs had already digitized, so no reset was necessary. The minimum dead time for an event that failed at level-3 was 8.5 μs. For every channel read into the energy sum module, this number increased by about 450 ns. This per-channel dead time was minimized by using only those cells of the calorimeter with a "low" discriminator over a threshold of 80 MeV. The total dead time incurred for a level-2 trigger that failed level-3 had a most-probable value in the range 10–12 μs, and an average of 15 μs under standard beam and trigger conditions. All events which passed the level-3 trigger were saved on permanent storage for subsequent off-line analysis.

4. Event reconstruction

4.1. LGD cluster finding

A photon incident on the LGD deposits energy in several LGD blocks. When these blocks are associated with each other, the position and energy of the incident photon can be estimated. In events with multiple photons, these clusters can overlap one another, leading to ambiguities
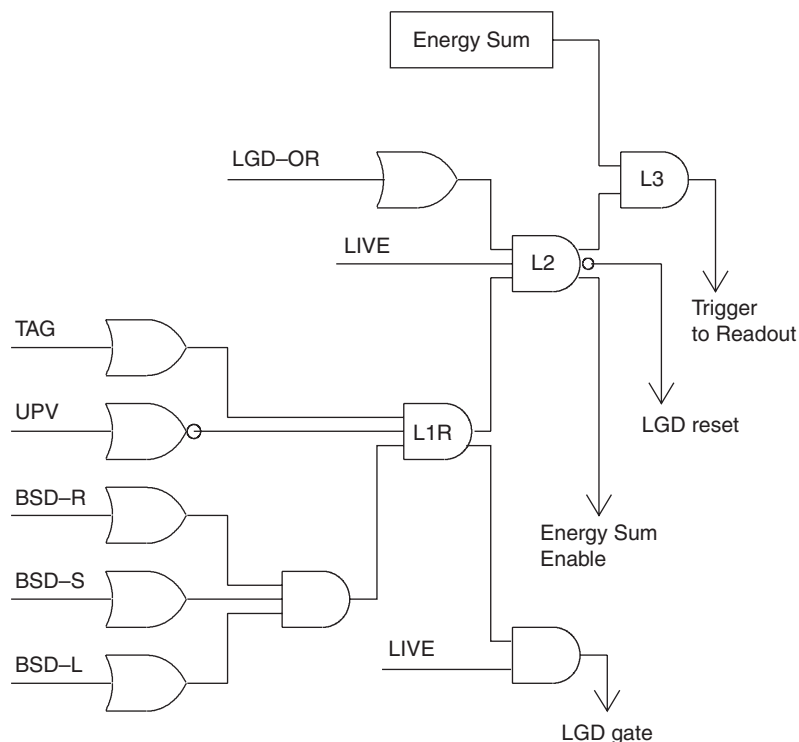

Fig. 3. The RADPHI trigger logic. L1R denotes Level-1 raw, Level-1 included L1R in coincidence with LIVE.

in the assignment of blocks to photons, and in some cases to the merging of two or more photons into a single reconstructed shower. On the other hand, statistical fluctuations in the distribution of energy between nearby blocks within a single shower can sometimes present the appearance of more than one overlapping shower, leading to the phenomenon of "split-off" photons. Thus the problem of interpreting an event in the LGD in terms of a discrete number of photon showers is a complex problem in pattern recognition. The following procedure was developed to optimize the trade-offs between shower merging and split-offs in the RADPHI experiment.

The algorithm to associate a group of blocks into "clusters" uses an iterative method that starts with the list of the LGD hits ordered by decreasing energy. At the beginning, all blocks above pedestal are considered "active", i.e. available for allocation to one or more clusters. The highest energy active block is taken as the seed for the first cluster, and that block is removed from the active list. Based on the energy and position of the seed block, a "new seed threshold" function is computed for each of the other blocks. Any blocks on the active list that are above the new-seed threshold function evaluated at their position are seed candidates for new clusters. The highest-energy seed candidate is taken as the seed of a new cluster. Then the new-seed threshold function is recomputed taking into account all clusters found so far, and the seed candidate list is updated. This process is continued until the highest energy seed candidate is below some seed energy cutoff, presently 40 MeV. At this point a complete list of clusters has been formed and the active list contains only non-seed blocks.

The next stage of cluster formation consists of assigning blocks from the active list to existing clusters. Each cluster is assigned an energy and position based on its seed, and a shower profile function is computed that estimates the expected energy in the surrounding blocks. All blocks in the active list with at least 1 keV of expected energy for a given cluster are allocated to that cluster's membership list. Any block which ends up being a member of more than one cluster has its energy partitioned between the competing clusters in the ratio of its expected energy for each. Execution of this step completes one iteration of the clusterization algorithm. Repeated iterations of this two-step procedure allow the full information of accumulated clusters to be used in subsequent passes to refine the estimates for shower position and energy that are used in computing the new-seed threshold and expected energy functions. The algorithm terminates when two subsequent iterations lead to the same cluster assignments. It was found that an average of five iterations was required for convergence.

The expected energy function of a cluster is given by

$$f_E(u,v) = E_C \exp\left\{ -\frac{1}{2}\left[\left(\frac{u-u_0}{\sigma_u}\right)^2 + \left(\frac{v-v_0}{\sigma_v}\right)^2 \right]^2 \right\} \quad (3)$$

where E_C is the cluster energy, (u,v) are the transverse coordinates of the block in question, and (u_0, v_0) are the corresponding coordinates of the cluster centroid. The u,v coordinate system is the laboratory x,y system rotated azimuthally such that $v_0 = 0$ and u_0 is positive. The value of σ_v is a constant approximately equal to the width of the LGD block, while $\sigma_u^2 = \sigma_v^2 + (8\theta)^4$ with σ_u, σ_v in cm and θ in radians. The θ-dependent term in σ_u was added to account for the obliqueness of showers at large polar angle.

The new-seed threshold function is computed as a sum over clusters, where each term in the sum is of the form

$$f_T(u,v) = 2E_s \exp\left\{ -\frac{1}{2}\left[\left(\frac{u-u_0}{\sigma_u}\right)^2 + \left(\frac{v-v_0}{\sigma_v}\right)^2 \right]^2 \right\}$$
$$+ [0.2 + 0.5\log(E_s + 1)]$$
$$\times \exp\left\{ -\frac{1}{2}\left[\left(\frac{u-u_0}{a_u}\right)^2 + \left(\frac{v-v_0}{a_v}\right)^2 \right]^{1/2} \right\} \quad (4)$$

where the E_s is the seed energy for the cluster in GeV, and a_u, a_v are similar in magnitude to σ_u, σ_v but have a small logarithmic dependence on the shower energy E_C. This functional form has the same behavior at small radius as Eq. (3) but includes an exponential tail to prevent shower off-shoots of limited magnitude at larger distances from the shower core from creating split-offs.

Once the energies and shower centroids of the reconstructed showers have been found, a non-linear transformation is used to convert these values to incident photon direction and energy. The method for determination of the energy and position of the photon from the reconstructed cluster has been described elsewhere [7].

4.2. BGD calibration and reconstruction

An initial gain equalization of the elements of the BGD was obtained using particles detected as pixels in the BSD. The distributions of ADC response from events with a single pixel in coincidence with a hit in the BGD were accumulated. Multiplication of the ADC values by a channel-dependent scaling factor made the observed ADC distributions identical. A Monte Carlo calculation was used to estimate the energy deposited in the BGD by a proton ejected from the target. This gave an overall factor (G) that allowed the ADC value observed in the BGD to be converted to GeV of deposited energy.

TDC information from a module allowed the effective speed of light in the module to be determined from pixel–calorimeter coincidences from the difference of the hit times from the two ends of the module divided by twice the speed of light in the fiber. This allowed the longitudinal position (z) of a BGD hit to be determined. Fitting the response as a function of the z-coordinate enabled extraction of the attenuation length (λ) for each module. Because the wavelength shifter readout significantly reduced the observed signal in the downstream end of the

detector the hit information from the downstream end was used only for time measurement.

Having G, z and λ enabled the shower energy to be computed from the upstream end ADC value in a barrel calorimeter module. The next step was to form clusters of hits in adjacent modules that agreed in time and z. After charged clusters in the BGD were masked off, the final calibration was performed in a similar fashion to the LGD calibration. Signals associated with known two-photon decays of the π^0 and η mesons were used to deduce the absolute energy calibration of the detector. In the case of the BGD the decay $\eta \to 2\gamma$ with one shower in the LGD and one in the BGD was used for an initial calibration. The decay $\pi^0 \to 2\gamma$ with both showers in the barrel was than used as a cross-check. The observed invariant masses agreed with their physical values. The observed widths of the η and π^0 in the barrel were 2–3 times larger than the widths observed in the LGD. For this reason the BGD was used only to veto events with large-angle showers in the off-line analysis.

5. Performance

5.1. Timing and rates

The RADPHI experiment ran for a total of about 1000 beam-hours. The tagged photon rate was 50 MHz. Data taking was divided into runs of 1–2 h duration. Data were saved on local disk and then migrated off-line to permanent storage on the Jefferson Lab Mass Storage System. An average of 350 events were collected by the data acquisition system per second. The average event record size was 600 bytes, leading to a modest data rate of 200 kB/s. The overall live-time achieved was 46%. For approximately the first half of the run period, a radiator of nominal 3×10^{-4} radiation lengths thickness was used with an electron beam current of 130 nA. For the second half the radiator thickness was increased to 6×10^{-4} radiation lengths and the electron beam current reduced to 77 nA. At a distance of 40 m from the radiator, the RADPHI target of diameter 2.87 cm intersected over 95% of the photon beam.

When the RADPHI target was moved out of the beam, rates in the detector scintillator elements dropped by about one order of magnitude.

All of the signals that are relevant to the event trigger are listed in Table 3. The gate for the ADCs and TDCs was generated from the level-1 trigger (see Fig. 3). The high rate in the *cpvOR* prevented its use as a veto in the on-line trigger. The total proton photoproduction cross-section integrated over the bremsstrahlung spectrum of the beam from pion threshold to the end-point leads to a total hadronic rate in the RADPHI target of 150 kHz. Increasing this rate by a factor of two to account for neutron photoreactions still does not approach the order of magnitude of the observed rates in the BSD and CPV.

GEANT-based Monte Carlo simulations of the RADPHI experiment, including the beam line, predict rates in

Table 3
Signal rates, widths and dead-time factors for the major components of the RADPHI detector

Signal	Rate (Hz)	Duration	Dead-time fraction
taggerOR	5.0×10^7	5 ns	0.07[a]
cpvOR	8.2×10^7		0.04[bd]
bgdOR	8.0×10^5		0.03[c d]
upvOR	0.9×10^6	40 ns	0.04
bsdORl	2.7×10^6	10 ns	0.002[e]
bsdORr	6.4×10^6	10 ns	0.005[e]
bsdORs	1.8×10^6	10 ns	0.001[e]
bsdAND	7.9×10^5	20 ns	0.016
Level-1[f]	5.8×10^5	10 ns	0.006
Level-2	2.7×10^5	1.2 μs[g]	0.31
Level-3	7.9×10^3	15 μs[h]	0.11
Readout	350	650 μs[i]	0.23

Rates shown are those obtained at full operating intensity.
[a] Based on 25 ns gate from individual channel discriminators.
[b] Based on 10 ns gate from individual channel discriminators.
[c] Based on 40 ns gate from individual channel discriminators.
[d] This is a veto inefficiency, no effect on experimental live-time.
[e] From 5 ns gate on individual channel discriminators.
[f] The level-1 logic signal before it is gated by the busy signal.
[g] Minimum dead time from receipt of level-1 gate to end of fast-clear when event fails level-2.
[h] Average dead time from receipt of level-1 gate to end of fast-clear when event passes level-2 and fails level-3.
[i] Average event readout time.

agreement with those shown in Table 3 coming from electromagnetic backgrounds alone. Most of the rate of charged particles coming from conversions originating in the target is confined to angles a few degrees from the beam but the tails of this distribution extend out as far as $60°$, accompanied by a diffuse omni-directional background of low-energy deltas and gammas. The energy distribution of this background peaks in the few MeV region, except in the area immediately surrounding the forward beam hole where the typical energies are tens of MeV. The hard component coming from pair conversions of energetic beam photons in the target escapes through the forward beam hole and does not affect the experiment. Evidence that soft electromagnetic backgrounds are the dominant contribution to the rates in the trigger counters is seen in the marked decrease shown in Table 3 going from the innermost BSD layer *bsdOR*-1 to the middle and outer layers. These three layers are in immediate contact with each other, with only the material of 5 mm of plastic plus two layers of tape shielding an outer layer from the flux seen by its inner neighbor. The fact that such a small amount of material led to a decrease in the observed rate by nearly a factor of two indicates that the background was primarily particles of a few MeV energies.

The hit rate in the BGD was a strong function of the discriminator threshold. During the early stages of the run, the BGD counters were operated at a low threshold corresponding to an electron-equivalent energy of 5 MeV. Under these conditions the total rate in the BGD was

800 kHz at standard operating intensity, as shown in the table. The BGD gains were lowered by a factor of 4 later in the run, effectively raising the thresholds to 20 MeV. This reduced the inclusive BGD rate to 120 kHz, in agreement with expectations based upon a total nuclear interaction rate of 300 kHz and 40% solid angle for the BGD acceptance. This observation is consistent with Monte Carlo simulations which show that the background rates in the barrel are dominated by hadronic sources for energies above 20 MeV. This is considered an effective lower bound on the energy of showers that may be reconstructed in the BGD.

There were no scalers or TDCs on the LGD signals so there is no direct measurement of the rates in the forward calorimeter. Instead these rates have been inferred from the increase with beam current in the average observed energy for a given block within the ADC gate. A minimum-bias trigger was formed using a coincidence of a signal in a BSD counter and the Hall B photon tagger. This trigger required an incident photon and a charged particle at a large angle to the photon beam. By deriving the trigger from barrel and tagger elements only, an unbiased view of what is happening in the forward detectors is obtained. This view contains two components, one which is correlated to the trigger in the barrel (hadronic events are likely candidates) and the other which is uncorrelated with the barrel and consists of random forward hits that happen to fall within the 100 ns ADC gate triggered by the barrel. These two components are distinguished by running two minimum-biased runs under unchanged beam conditions, one at full beam intensity (77 nA) and the other at low intensity (2 nA).

The rate in a block is defined as the fraction of events for which the block's ADC is over threshold divided by the gate width. This rate is the sum of the barrel-correlated component which does not depend on beam current (a constant probability divided by a constant gate width) and the barrel-accidental part which is linear in beam current and disappears in the limit of low rate. When the beam current was reduced from 77 to 2 nA the rates across the LGD decreased by only a factor of about 8 instead of the factor of 38 expected if only accidentals were present. On the other hand, if only barrel-correlated hits were present in the LGD then this rate should have been independent of beam current. This shows that at 77 nA the LGD inclusive rates are accidentals-dominated and at 2 nA they are dominated by the barrel-correlated component.

Within errors, the inclusive LGD rate that would be measured on a free-running scaler connected to each block is simply the difference in the above-defined block rates between the high- and low-intensity runs. These rates are plotted as the data points in Fig. 4a as a function of the distance of the block from the beam axis. The histogram in the figure is the Monte Carlo estimate for the LGD rates arising only from electromagnetic background. Note that the expected hadronic rate for individual blocks is negligible on this scale. The excess of the data over Monte
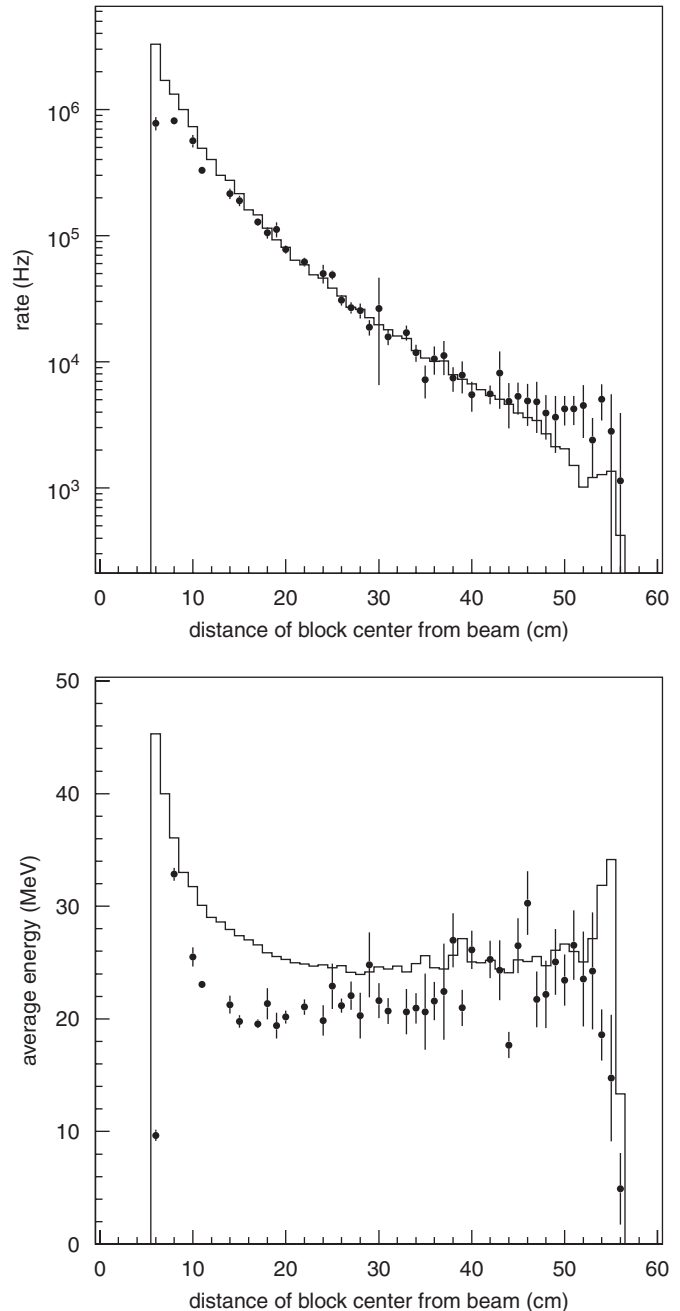

Fig. 4. Characteristics of unbiased flux observed in individual blocks in the LGD as a function of distance from the beam. The points are derived from data and the histograms from a Monte Carlo simulation of the electromagnetic background coming from the beam and target. Rates (first panel) and average energy (second panel) include all hits over 15 MeV.

Carlo at large radius suggests that there are sources of background in the experimental hall that are not included in the simulation. The simulation includes the principal components of the Hall B photon beam line starting at the radiator and ending at the downstream yoke aperture. An excellent agreement between observed and predicted rates is seen across most of the face of the LGD. The ADC threshold used in the Monte Carlo for this comparison is 15 MeV, which corresponds roughly to the on-line

threshold that was applied to the LGD data by the data acquisition.

Note that in Fig. 4a marked rate depression appears at small radius, relative to the predicted rates. These blocks are in the vicinity of the beam hole. In addition to suffering from the highest rates, these blocks also sustained the greatest radiation damage. The eight blocks closest to the beam axis (first data point) are the most affected, but some effects can be seen at neighboring points. These data which were taken toward the end of the RADPHI run period provide a quantitative measure of the effects of radiation damage on the response of the LGD. More insight can be provided by the pulse-height spectrum of these background hits in the minimum-bias sample. All of the spectra show a maximum intensity at threshold and an exponential tail that extends to the GeV region. The mean of this distribution is plotted in Fig. 4b as a function of block distance from the beam axis. As in Fig. 4a the points are the data and the histogram is the Monte Carlo prediction. The comparison is sensitive to the exact threshold used, which was 15 MeV for Monte Carlo but varied between 10 and 20 MeV for real data, depending on the channel. Even with this caveat, the general trends are very similar between data and Monte Carlo, including the forward rise that is expected based upon the kinematics of electromagnetic showers. The depression of the response of the innermost blocks is due in part to radiation damage, but also to the fact that these blocks contained so much background that the calibration procedure tended to artificially suppress their gains relative to their neighbors in the interest of optimizing the total shower energy resolution.

5.2. Photon tagging at high rates

Nominal operating conditions called for an inclusive rate of 5×10^7 γ/s in the tagged range from 77% to 95% of the end-point energy. The electronic sum of the signals from the 19 tagging counters, called the *taggerOR*, was included in the level-1 trigger to ensure that every event had a hit in at least one tagging counter within the on-line tagging coincidence window of 20 ns.

By conventional standards for tagged photon experiments, 5×10^7 Hz is a high tagging rate that requires special care in the treatment of accidental coincidences. On average, within the on-line coincidence window of 20 ns, one accidental tagging coincidence is expected in addition to any true coincidence that might be present for a given event. After the timing differences between channels have been eliminated in the off-line analysis and the timing resolution optimized by correcting for signal propagation delays, the coincidence window was reduced to a few ns. At this point the accidental probability is reduced to approximately 30%. However, accidental tags can still outnumber the true tags because the level-1 trigger was dominated by background. Approximate conditions for the RADPHI analysis were that only 10% of the experimental triggers corresponded to actual tagged photons interacting

in the target. This led to a ratio of 3:1 in accidental/true coincidences in the tagged event sample. The correct treatment of these accidentals is to apply the delayed coincidence subtraction technique that will be described below.

The reference time for an event was derived from the BSD where a hit from one charged track, presumably the recoil proton, was required by the trigger. The light-propagation time was subtracted from the times of the hits in each of the three counters forming the pixel. The average of these three corrected times for a given pixel is called the "pixel time." Taken relative to the tagger, the pixel time measures the time-of-flight for the recoil particle. An average time-of-flight of 5 ns/m is subtracted from the pixel time to form the "recoil time." Defined in this way, the recoil time gives an optimum time resolution of the BSD relative to the tagger.

Rates in individual CPV counters were a few MHz but the summed rate of the entire CPV was over 80 MHz. In the off-line analysis, a CPV was applied by eliminating all events for which any CPV hit fell within a certain time window with respect to the recoil time. A veto window of 6 ns width was sufficient to contain the entire CPV–BSD coincidence peak at a cost of only 30% in accidental vetos.

Fig. 5 shows the time difference between the tagger and recoil hits. All tagger hits are treated on the same footing, leading on average to more than one entry in the spectrum per event. In the case where more than one barrel pixel is present in an event, the earliest pixel defines the recoil time. The regularly spaced spikes in the spectrum are significant; they reflect the 2 ns period of the CEBAF beam. Thus, the coincidence peak is related to one leading and two adjacent beam buckets. The dashed histogram in Fig. 5 results when the CPV is applied. The shaded area under the peak shows recoils which are identified with neutral tagged coincidences while the shaded area to the right of the peak represents those that are used for subtraction of accidentals.

The power of this combined CPV-tagging analysis to isolate a clean sample of neutral γ, p events is demonstrated by the quality of the total energy signal seen in the forward calorimeter in association with a single tagging counter. The first panel of Fig. 6 shows the summed energy of all reconstructed showers in the forward calorimeter, for events with a single recoil and no extra charged or neutral energy in the barrel. These spectra demonstrate that a simple event-by-event tagging analysis is ineffectual at these high rates. The dashed histogram is filled for all events that contain at least one coincidence with a selected tagging counter at the high-energy end of the tagger around 5.36 GeV, while the solid histogram is taken in coincidence with a tagging counter at the low end of the tagged range around 4.41 GeV. Little difference can be seen between the two spectra apart from a shoulder on the high side of the peak in the case of the higher-energy counter. The second panel shows the same two spectra after the application of the CPV-tagging analysis described above,
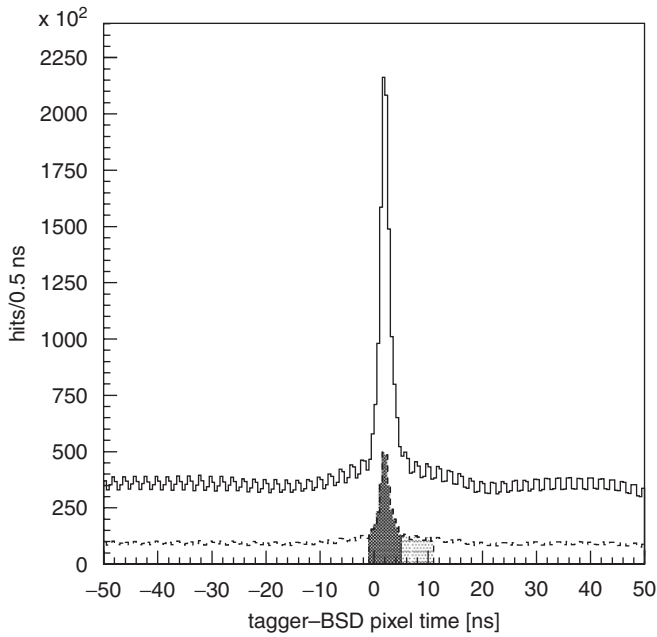
Fig. 5. Spectrum of the tagger time relative to the recoil. The solid histogram includes all events, while the dashed one refers only to those that have no CPV hit within the veto window. The shaded regions indicate the windows used to remove accidental tags by the delayed coincidence technique.

applied to the same two tagging counters. The vertical lines indicate the expected median energy of the beam spectrum subtended by the respective tagger channels, based upon the known electron beam energy and the field in the spectrometer. A downward shift of about 100 MeV and a tail to lower energies is expected in these spectra because of the energy from the incident photon that is carried away by the recoiling target. This agreement between expectation and measurement in the total energy scale was obtained without fine-tuning, purely on the basis of the LGD calibration that adjusted the observed 2γ mass peaks to align with the physical masses of the π^0 and η.

The counting rates in the two tagging counters shown in Fig. 6 are roughly equal. The difference in the tagged yields for the two counters that is seen in the second panel reflects the decrease in the cross-section times acceptance for 1-prong reactions across the photon energy range of the tagger.

The importance of accidentals subtraction in the tagging analysis is illustrated in Fig. 7. Only events reconstructed with two clusters in the LGD are included in this sample. The upper open histogram is the total forward energy spectrum for all events in coincidence with a selected tagging counter near the middle of the tagged range. The anti-coincidence with the CPV has been applied. The shaded histogram shows the same spectrum after tagger accidentals have been subtracted, giving the tagged spectrum for that tagging counter. The curve through the tagged spectrum is a fit to the sum of two Gaussians, one representing the central peak and the other associated with
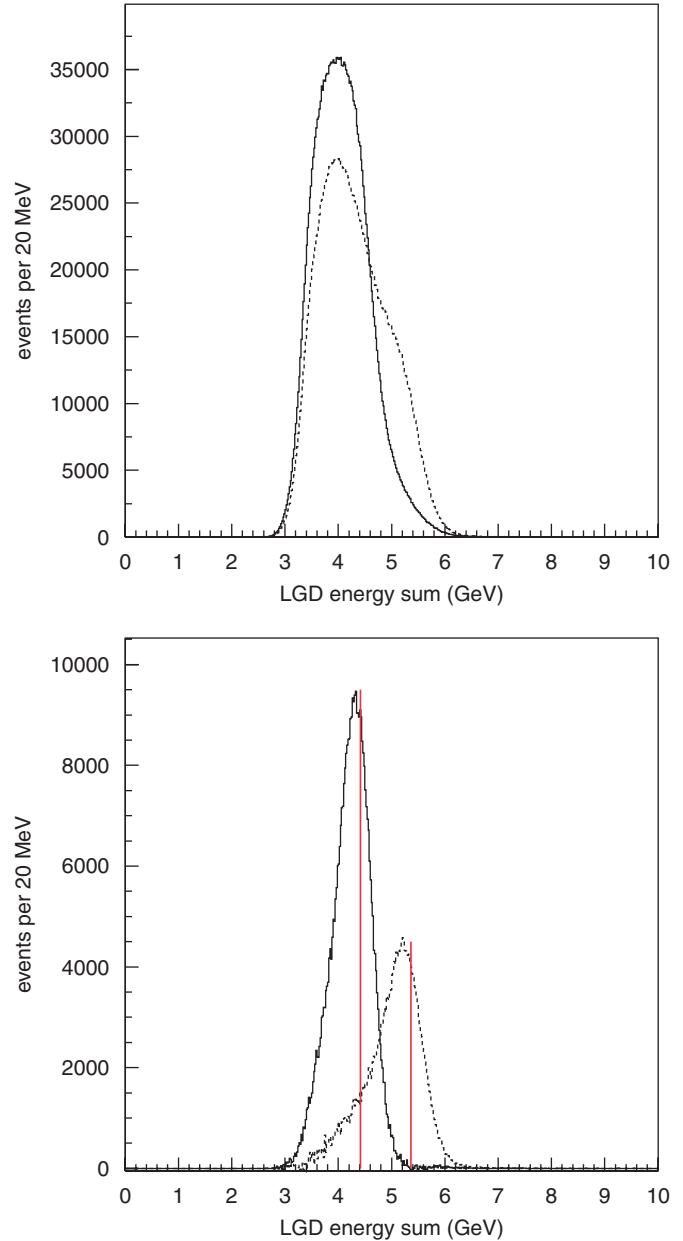

Fig. 6. Summed energy from all reconstructed forward clusters in an event. The sample includes all events with between 2 and 7 clusters, a single recoil and no extra energy in the barrel. The first panel shows the spectrum corresponding to events in coincidence with tagging counter 19 (solid histogram) at the low-energy end of the tagged photon range and counter 1 (dashed histogram) at the high-energy end. The second panel shows the same two spectra after the CPV-tagging analysis described in the text has been carried out for the same two tagging counters. The vertical lines indicate the beam photon energy associated with the given tagging counter.

the low-energy tail. The r.m.s. width of the central peak is 280 MeV, in good agreement with expectations based on the observed energy and position resolution of the LGD.

5.3. Yields

The integrated live-time of the experiment under standard operating intensity and trigger was 1.56×10^6 s

corresponding to an integrated luminosity of 18.9 pb^{-1} in γ^9Be interactions within the tagged region of the beam photon spectrum. If nuclear corrections may be neglected, this corresponds to 75.6 pb^{-1} in γp interactions. The trigger acceptance for γp $\rightarrow$ pX reactions where X decays to all-neutral final states is on the order of 50%, where losses come mainly from absorption of recoil protons in the target and escape of final-state photons through the forward hole in the calorimeter.

The total numbers of events collected and reconstructed at successive stages in the analysis are shown in Table 4,
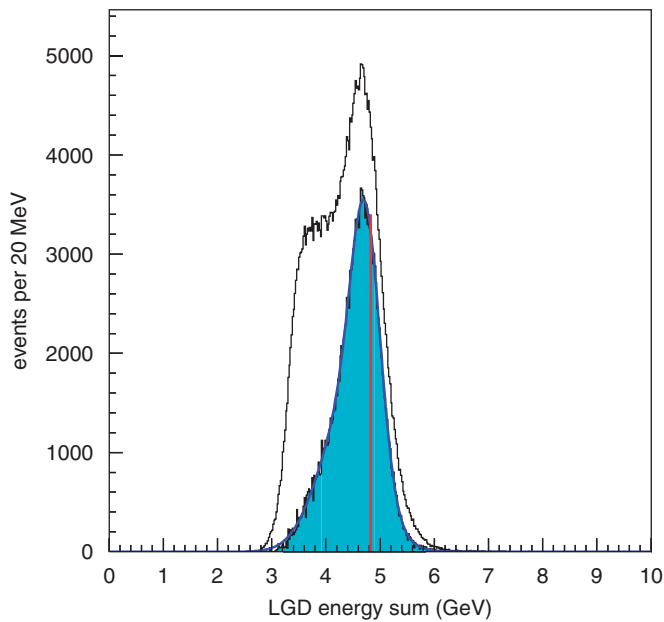
Fig. 7. Summed energy from all reconstructed forward clusters in an event before (open histogram) and after (shaded histogram) tagging accidentals have been subtracted. Only tagging channel 10 was included in the analysis, corresponding to a 50 MeV bin in the beam energy spectrum centered at the position of the vertical line. The sample includes all events with exactly two reconstructed clusters, a single recoil and no extra energy in the barrel. The curve is a fit to the sum of two Gaussians.

broken down according to the shower multiplicity in the forward calorimeter. The selection criteria are applied sequentially, that is, events counted in a given row in Table 4 satisfy the criteria listed in all rows above it.

The first requirement (Cluster energy) was that no reconstructed cluster have an energy less than 50 MeV and that the total energy of all reconstructed clusters be greater than 3.0 GeV. The first part suppressed background associated with the beam, while the second refined the hardware trigger processor requirement to a fixed, known value. The second requirement (1-prong) demanded exactly one pixel cluster in the BSD. Two adjacent pixels were merged together into a pixel cluster if they occurred within 3 ns of each other. The pixel cluster was required to be within 10 ns of the event trigger. This requirement (CPV) served to select events with a single recoiling charged particle, assumed to be a proton. The next requirement rejected events with any hit in the CPV within 3 ns of the pixel cluster. Events with forward charged particles were rejected by this requirement. The event yields listed as "tagged" in the table are the numbers of events after accidental tagging subtraction discussed above.

The next requirement was that showers with an energy less than 0.5 GeV satisfy

$$E + A\theta > B \qquad (5)$$

with $A = 0.13$ GeV/degree and $B = 1.033$ GeV. The numbers A and B were chosen to reduce the observed electromagnetic background that peaked at low angles and energies. The final requirement was that there be no showers reconstructed in the BGD. BGD clusters found to be correlated in space with the pixel cluster were not considered. This requirement rejected poorly contained events. Examples of neutral decays reconstructed by the detector can be seen in Figs. 8–11.

Fig. 8 shows the 2γ invariant mass distribution from events with two reconstructed showers with the cuts listed in Table 4 applied. The inset of Fig. 8 shows the region near the mass of the η. A background is visible in the inset.

Table 4
Event yields at successive stages in the RADPHI analysis, broken down according to shower multiplicity in the forward calorimeter

Sample	2γ	3γ	4γ	5γ	6γ	7γ
On tape	2.17×10^8	2.40×10^8	2.09×10^8	1.41×10^8	7.83×10^7	3.72×10^7
Cluster energy[a]	2.02×10^8	2.20×10^8	1.93×10^8	1.32×10^8	7.31×10^7	3.46×10^7
1-prong[b]	1.28×10^8	1.35×10^8	1.21×10^8	8.55×10^7	4.79×10^7	2.26×10^7
CPV[c]	6.84×10^7	5.44×10^7	4.25×10^7	2.53×10^7	1.35×10^7	6.24×10^6
Tagged[d]	2.23×10^7	1.37×10^7	9.76×10^6	4.08×10^6	1.64×10^6	5.35×10^5
Fiducial cut[e]	2.13×10^7	1.05×10^7	7.47×10^6	2.46×10^6	9.71×10^5	2.85×10^5
Barrel γ veto[f]	1.32×10^7	5.50×10^6	4.32×10^6	1.22×10^6	4.41×10^5	9.66×10^4

[a] All clusters > 0.05 GeV, total energy > 3.0 GeV.
[b] Single isolated hit in barrel scintillators.
[c] No in time hits in CPV.
[d] After accidental subtraction.
[e] Cluster energy/angle requirement.
[f] No showers reconstructed in the BGD.

This background is due to $\omega \to \pi^0\gamma \to 3\gamma$ where either two of the three photons were less than 6 cm apart and were merged into a single cluster, or a low energy photon somehow escaped detection.

Fig. 9 shows the invariant mass distribution from events with three reconstructed showers. The solid histogram shown in the left plot was obtained from this sample after the application of the cuts discussed above. The $\omega \to 3\gamma$ signal is visible as the peak near 0.8 GeV. The two lower mass peaks are associated with 2γ decays of π^0 and η mis-

reconstructed as 3γ by the addition of an accidental low-energy shower that survives the cuts. Selecting events with $\pi^0\gamma$ kinematics by requiring that one of the pairs from the 3γ sample is consistent with the π^0 mass suppresses contamination from this type of background while preserving the ω signal. The result of applying this requirement is shown as the dashed histogram.

The plot on the right of Fig. 9 shows the signal associated with $\phi \to \eta\gamma$. The solid histogram shows the spectrum obtained by requiring one pair of photons to have an effective mass consistent with $\eta \to 2\gamma$. The background, in this case approximately as large as the signal, was suppressed by the additional requirement that the total energy in the LGD be within 300 MeV of the tagged photon energy (dashed histogram). The solid curve superimposed on the dashed histogram is a fit to a sum of two Gaussians plus a second order polynomial. The shaded area, formed from the sum of the wider Gaussian and the polynomial, represents the background. The peak position and width of the remaining Gaussian are consistent with the nominal ϕ mass and expected mass resolution in the LGD, respectively.

Fig. 10 shows evidence for $\gamma p \to b_1(1235)p$ followed by the decay $b_1(1235) \to \omega\pi^0$ and $\omega \to \pi^0\gamma$. Events for this figure were required to have one and only one arrangement of photons consistent with the hypothesis $\pi^0\pi^0\gamma$, exactly one pixel in the BSD, exactly one hit in the tagger consistent in time with the pixel and a total energy deposition in the LGD greater than 4.3 GeV. The first panel shows the $\pi^0\gamma$ effective mass from events satisfying the selection criteria (two combinations per event). The prominent structure is centered at the mass of the ω. The second panel is the $\pi^0\pi^0\gamma$ effective mass vs. the $\pi^0\gamma$ effective mass (two combinations per event). The enhancement seen between the vertical lines has a $\pi^0\pi^0\gamma$ mass peaking near
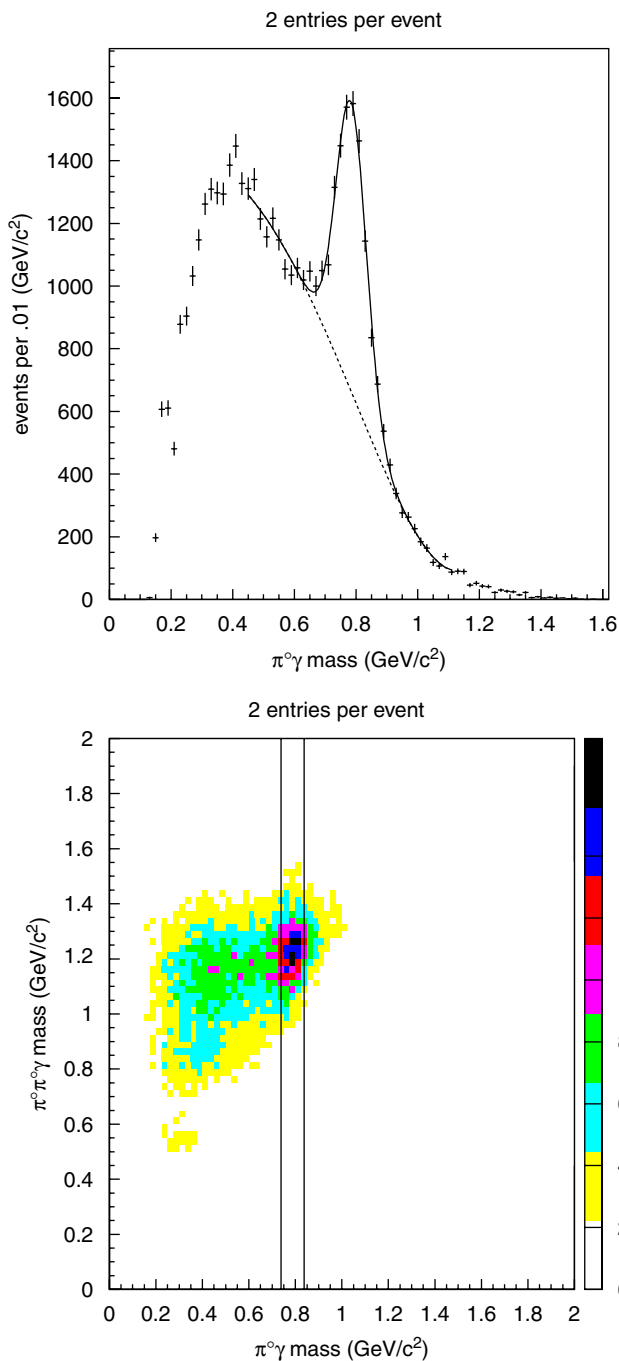

Fig. 8. The effective mass spectrum derived from events with exactly two reconstructed showers in the forward calorimeter. The criteria discussed in the text and Table 4 have been applied. Clearly visible are peaks associated with $\pi^0 \to 2\gamma$ and $\eta \to 2\gamma$ (the inset shows this region in detail).

Fig. 9. The effective mass spectrum derived from events with exactly three reconstructed showers in the forward calorimeter. The left panel shows the spectrum after all cuts in Table 4 have been applied. The solid histogram is all events, while the dashed histogram has the additional requirement that one pair of photons has an effective mass consistent with $\pi^0 \to 2\gamma$. Evidence for the decay $\omega \to \pi^0\gamma$ is clearly seen. The right panel shows the spectrum after applying all the cuts in Table 4 and also requiring that one pair of photons is consistent with $\eta \to 2\gamma$. The dashed histogram in the right panel results when the total reconstructed shower energy is required to be within 0.3 GeV of the beam energy derived from the tagger. Evidence for the decay $\phi \to \eta\gamma$ is seen.
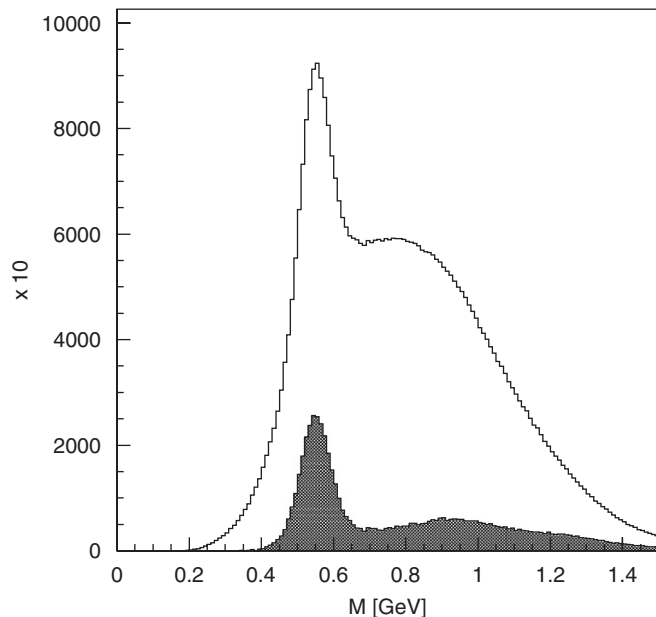
Fig. 11. Invariant mass of six showers reconstructed in the LGD. The solid histogram is obtained after applying all cuts listed in Table 4 except the tagging accidentals subtraction. The shaded histogram results when the tagging analysis is included.

Fig. 10. The 3γ effective mass distribution from events identified as $\pi^0\pi^0\gamma$ is shown in the first panel. The prominent structure is due to the decay $\omega \to \pi^0\gamma$. The second panel shows the $\pi^0\pi^0\gamma$ mass vs. the $\pi^0\gamma$ mass. The structure between the vertical lines (centered on the ω mass) is due to the production of the $b_1(1235)$ meson followed by its decay to $\pi^0\pi^0\gamma$ via $\omega\pi^0$.

$1.235\,\mathrm{GeV}/c^2$, the nominal mass of the b_1 and a $\pi^0\gamma$ effective mass at the mass of the ω. Further details of the selection criteria and analysis can be found in Ref. [10].

Fig. 11 shows the invariant mass of six reconstructed showers. The solid histogram was obtained after applying the 1-prong requirement, CPV, BG veto and LGD fiducial cut. The $\eta \to 3\pi^0 \to 6\gamma$ decay is clearly visible. The shaded histogram is obtained after applying tagging accidental

subtraction. This leaves the η signal almost without background, which confirms the proper application of the tagging analysis in high, as well as in low, multiplicity events.

6. Conclusions

We have described the operation and performance of the RADPHI detector. The on-line trigger and reconstruction algorithms developed worked well in the challenging, high rate-environment of $5 \times 10^7\,\mathrm{s}^{-1}$ tagged bremsstrahlung photons. A 3-level trigger was employed to select $\gamma\mathrm{p} \to \mathrm{p}X$ reactions with X being a meson decaying into an all-photon final state. The purpose of the experiment was to detect radiative decays of vector mesons, with the ultimate goal of searching for rare decays of the ϕ into $f_0(980)\gamma$ and $a_0(980)\gamma$. During a 1000 h run in the year 2000 the experiment collected over 10^9 triggers, from which approximately 2M radiative vector meson decay events have been reconstructed including $\omega \to \pi^0\gamma$ and $\phi \to \eta\gamma$.

Calibration of the two calorimeters (LGD and BGD) used to detect photons was performed utilizing 2γ decays of π^0 and η mesons. Observed meson masses agreed very well with their nominal values and their widths were consistent with the resolutions of the respective calorimeters.

The rates in the scintillation detectors BSD and CPV exceeded expected hadronic rates based on the total hadronic photoproduction cross-section by several orders of magnitude. GEANT-based Monte Carlo simulations of the RADPHI experiment were able to reproduce observed rates by taking into account electromagnetic background

alone. High rates in the CPV prevented its use in the on-line trigger.

The rates in the LGD were extracted by dividing the fraction of events for which the block's ADC was over threshold by the gate width, and comparing the results from high- and low-intensity minimum-bias runs. These indirectly measured rates in the LGD also agreed very well with Monte Carlo predictions, except for the innermost blocks that sustained substantial radiation damage.

Successful performance of the RADPHI detector is confirmed by the off-line analysis that was devised to isolate physical signals in the presence of the high-level background. In order to enhance signals from peripheral γp interactions with all-photon final states contained in the forward calorimeter, a single charged track at lab polar angles greater than $30°$, no beam-associated low energy showers in the LGD and no showers in the BGD were required. Events with charged particles in the forward region were eliminated by the CPV. A method for tagging high-intensity photons in the case when there was no time information to correlate the signal in the LGD with the trigger proved very important. It enabled an independent cross-check of the LGD energy calibration and resolution. Final states with as many as six photons were successful reconstructed. These include $\pi \rightarrow 2\gamma$, $\eta \rightarrow 2\gamma$, $\omega \rightarrow \pi^0\gamma \rightarrow 3\gamma$, $\phi \rightarrow \eta\gamma \rightarrow 3\gamma$, $b_1 \rightarrow \omega\pi^0 \rightarrow 5\gamma$ and $\eta \rightarrow 3\pi^0 \rightarrow 6\gamma$. All identified meson peaks in the invariant mass distributions agreed with their nominal values. Their widths reflect the mass resolution of the detector, in agreement with expectations from Monte Carlo.

Acknowledgments

References

[1] A Measurement of Rare Radiative Decays of the ϕ Meson. J Lab Experiment E-94-016.
[2] D.I. Sober, et al., Nucl. Instr. and Meth. A 440 (2000) 263.
[3] The Science and Experimental Equipment for the 12 GeV Upgrade of CEBAF, Jefferson Lab pCDR, 2004. URL 〈http://www.jlab.org〉.
[4] W.-M. Yao, et al., J. Phys. G, 33 (2006) 1. URL 〈http://pdg.lbl.gov〉.
[5] D.W. Hertzog, et al., Nucl. Instr. and Meth. A 294 (1990) 446.
[6] M. Dahmen, et al., Nucl. Instr. and Meth. A 348 (1994) 97.
[7] R.T. Jones, et al., Nucl. Instr. and Meth. 566 (2006) 366.
[8] S. Teige, et al., Phys. Rev. D 59 (1999) 012001.
[9] R.R. Crittenden, et al., Nucl. Instr. and Meth. A 387 (1997) 377.
[10] C.P. Steffen, Probing meson structure using photoproduction, Ph.D. Thesis, Indiana University, Bloomington, Indiana, 2001, unpublished.